Supporting Information

Cathodic Corrosion-Induced Structural Evolution of CuNi Electrocatalysts for Enhanced CO_2 Reduction

Wenjin Sun [1,†], Bokki Min [2,†], Maoyu Wang [3], Xue Han [4], Qiang Gao [1], Sooyeon Hwang [5], Hua Zhou [3], and Huiyuan Zhu [1,2,*]

[1] Department of Chemistry, University of Virginia, Charlottesville, VA 22904, US
[2] Department of Chemical Engineering, University of Virginia, Charlottesville, VA 22904, US
[3] Advanced Photon Source, Argonne National Laboratory, Lemont, IL 60439, US
[4] Department of Chemical Engineering, Virginia Polytechnic Institute and State University, Blacksburg, VA 24061, US
[5] Center for Functional Nanomaterials, Brookhaven National Laboratory, Upton, NY 11973, US
* Correspondence: kkx8js@virginia.com
† These authors contributed equally to this work.

Received: 22 October 2024; Revised: 25 November 2024; Accepted: 27 November 2024; Published: 4 December 2024

Experimental Section:

Chemicals and Reagents

Copper (II) acetylacetonate ($Cu(acac)_2$, 99.99%), nickel (II) acetylacetonate ($Ni(acac)_2$, 99.99%), oleylamine (OAm, 70%), trioctylphosphine (TOP, 99%), potassium bicarbonate ($KHCO_3$, 99.7%), 3-(trimethylsilyl) propionic-2,2,3,3-d4 acid sodium salt (NMR internal standard) and Nafion perfluorinated resin solution (5 wt%) were purchased from Sigma Aldrich (Burlington, MA, US). The Nafion-117 membrane, Vulcan XC carbon black and AvCarb carbon paper were purchased from Fuel Cell Store (Bryan, TX, US). All chemicals were used without further purification. Argon (99.99%), carbon dioxide (99.999%) was purchased from Linde (Danbury, CT, US).

Synthesis of Core-Shell Cu_xNi_{1-x} Nanoparticles (NPs)

A modified procedure was used to synthesize Cu_xNi_{1-x} NPs [1]. Taking $Cu_{0.7}Ni_{0.3}$ for example, 0.7 mmol $Cu(acac)_2$, 0.3 mmol $Ni(acac)_2$, and 10 mL OAm were added into a 50 mL four-necked flask under stirring. The mixture was then heated to 80 ℃ under a N_2 atmosphere and kept for 30 min. Subsequently, 2 mL TOP was added to the solution. The system was heated to 220 ℃ at a ramping rate of 10 ℃/min and maintained at this temperature for 2 h, producing a brownish solution. After cooling down to room temperature, the precipitate was centrifuged and washed three times with hexane and excess ethanol, then redispersed in hexane. Cu_xNi_{1-x} NPs with different composition ratios were synthesized using the same procedure with the corresponding precursor ratios.

Characterization

The morphology and size of the as-synthesized Cu_xNi_{1-x} NPs were characterized using transmission electron microscopy (TEM) on a Philips EM420 (Thermo Fisher Scientific, Waltham, MA, US), operated at 120 kV. X-ray diffraction (XRD) patterns were collected by a Philips X'Pert Pro Super (Philips Analytical, Westborough, MA, US) with Cu Kα (λ = 1.5406 Å). Inductively coupled plasma optical emission spectroscopy (ICP-OES) was performed for quantitative elemental analysis on a SPECTRO GENESIS ICP spectrometer (AMETEK, Hudson, NH, US). Scanning transmission electron microscopy combined with electron energy loss spectroscopy (STEM-EELS) were conducted on a Hitachi HD2700C with Gatan 977 Enfinium ER spectrometer (Hitachi, Tokyo, Japan). In-situ X-ray absorption near-edge spectroscopy (XANES) and Fourier-transformed extended X-ray absorption fine structure (EXAFS) experiments were carried out at beamline 12BM-B, Advanced Photon Source, Argonne National Laboratory. The working electrodes were prepared by depositing catalysts on ~ 100 μm-thick carbon fiber paper. The catalyst electrode was mounted onto a custom-designed in-situ XAS fluorescence cell, as described in previous study [2]. The same counter electrode, reference electrode, and electrolyte were used as described in the Electrochemical measurement's session. During the in-situ and operando XAS measurements, CO_2 was constantly bubbled. All data were collected in a fluorescence mode under various applied potentials controlled by a Biologic SP-200 workstation (BioLogic Science Instruments, Knoxville, TN, US). A 13-Element Ge detector was used to

collect the Cu and Ni K fluorescence signal. Each selected potential was held until enough data statistics of XAS were achieved. The X-ray beam was calibrated using both Cu and Ni metal foil. Data reduction, data analysis, and EXAFS fitting were performed with the Athena and Artemis software packages [3]. Standard procedures were used to extract the EXAFS data from the measured absorption spectra. For quantitative EXAFS analysis, Cu and Ni metal were fitted as the reference samples to obtain the amplitude reduction factor (S02) values. With S02 known, the EXAFS data of the catalyst materials were fitted with such generated amplitudes to obtain coordination numbers.

Preparation of Ink and Electrode

Ink preparation: To load Cu_xNi_{1-x} NPs on carbon, 10 mg of the as-synthesized Cu_xNi_{1-x} NPs were sonicated with 40 mg activated carbon (Vulcan XC-72R, Cabot Corporation, Boston, MA, US) in hexane for 2 h [4]. The mixture was then centrifuged at 8500 rpm for 5 min. To remove the organic ligand, the catalysts were immersed in a mixture of 1.5 mL hydrazine and 18.5 mL ethanol and stirred overnight. The catalysts were then washed with excessive ethanol twice and dried in a vacuum oven at 50 °C for 4 h. To prepare the ink, 10 mg of Cu_xNi_{1-x}/C catalyst powder was mixed with 2 mL of isopropanol and 40 μL of Nafion solution, followed by sonication for 30 min to form a homogeneous solution. All catalyst inks in this work were prepared using the same procedure.

Electrode preparation: The as-prepared catalyst inks were airbrushed onto a carbon paper and allowed to dry naturally before use, achieving a Cu_xNi_{1-x}/C loading of 1 mg cm^{-2}.

Electrochemical Measurement and Product Analysis

Electrochemical measurements were all carried out in 0.1 M $KHCO_3$ using a Biologic electrochemical workstation to control all potential. The H-type gas-tight cell was separated by a Nafion 117 membrane, with each compartment containing 40 mL of 0.1 M $KHCO_3$. A platinum foil and an Ag/AgCl (3.5 M KCl) were used as the counter and reference electrodes, respectively. Cyclic voltammograms (CV) were recorded in an Ar-saturated electrolyte solution between −2.0 V and −0.6 V *vs*. Ag/AgCl after 20 cycles, at a scan rate of 20 mV s^{-1} at room temperature, and subsequently in a CO_2-saturated electrolyte under the same condition. For electrodes requiring activation, a cathodic activation step was performed for 2 h. Chronoamperometry (CA) measurements were carried out at potentials from −1.6 V to −2.0 V *vs.* Ag/AgCl for 1 h in the H-type cell system. All the potential was then converted to the reversible hydrogen electrode (RHE) reference scale according to E (vs. RHE) = E (*vs*. Ag/AgCl) + 0.198 V + 0.059 × pH. The reported current densities were normalized to geometric surface areas. Gas products were analyzed using gas chromatography (Agilent 7890 B) equipped with a thermal conductivity detector and a flame ionization detector. Liquid products were analyzed by ^{1}H NMR (Bruker Advance II 500M, Billerica, MA, US) with 3-(trimethylsilyl) propionic-2,2,3,3-d_4 acid sodium salt as an internal standard.

The Calculation of Faradaic Efficiency (FE):

The FEs of gas products were calculated by [5]:

$$FE_{gas}(\%) = \frac{A}{\alpha} \times Vco_2 \times \frac{n \times F \times p_0}{RT} \times (Electrode\ area)^{-1}$$

where α is the conversion factor based on the calibration of the GC with the standard samples of each gas products, respectively. V_{CO2} is the CO_2 flow rate (10 sccm); F is the Faraday constant (96,485 C· mol^{-1}); p_0 is the pressure (1 atm); T is the temperature (273 K); R is the gas constant (82.1 mL· atm· K^{-1}· mol^{-1}); A is the peak area of the gas product obtained from GC. *FE* for the various gas products was obtained by dividing the partial current density by the total current density.

The liquid product was analyzed by NMR. To prepare the NMR sample, 0.5 mL electrolyte containing the liquid product was mixed with 0.1 mL D_2O and 0.1 mL 0.1 M 3-(trimethylsilyl) propionic-2,2,3,3-d_4 acid sodium salt (internal standard). The FE of liquid product was given by [5]:

$$FE_{liquid}(\%) = \frac{N \times n \times F}{Q_{total}} \times 100$$

where N is the number of moles of liquid product formed during CO_2RR, n is the number of mole of electron required for *1* mol of product formation, F is 96485 C/mol (Faraday constant), and Q_{total} is the total charge passing during reaction.

The partial current density is calculated through multiplying the total geometric current density by the faradaic efficiency for each product at a given potential as following [6]:

$$j_{C2+} = \frac{j_{total} \times FE_{c2+}}{a};$$

$$j_{H2} = \frac{j_{total} \times FE_{H2}}{a}$$

where j_{C2+} and j_{H2} are the partial current density of C_{2+} products and H_2, respectively; j_{total} is the total current density during reaction, a is the geometric surface area, which is 1 cm^2 in our system.

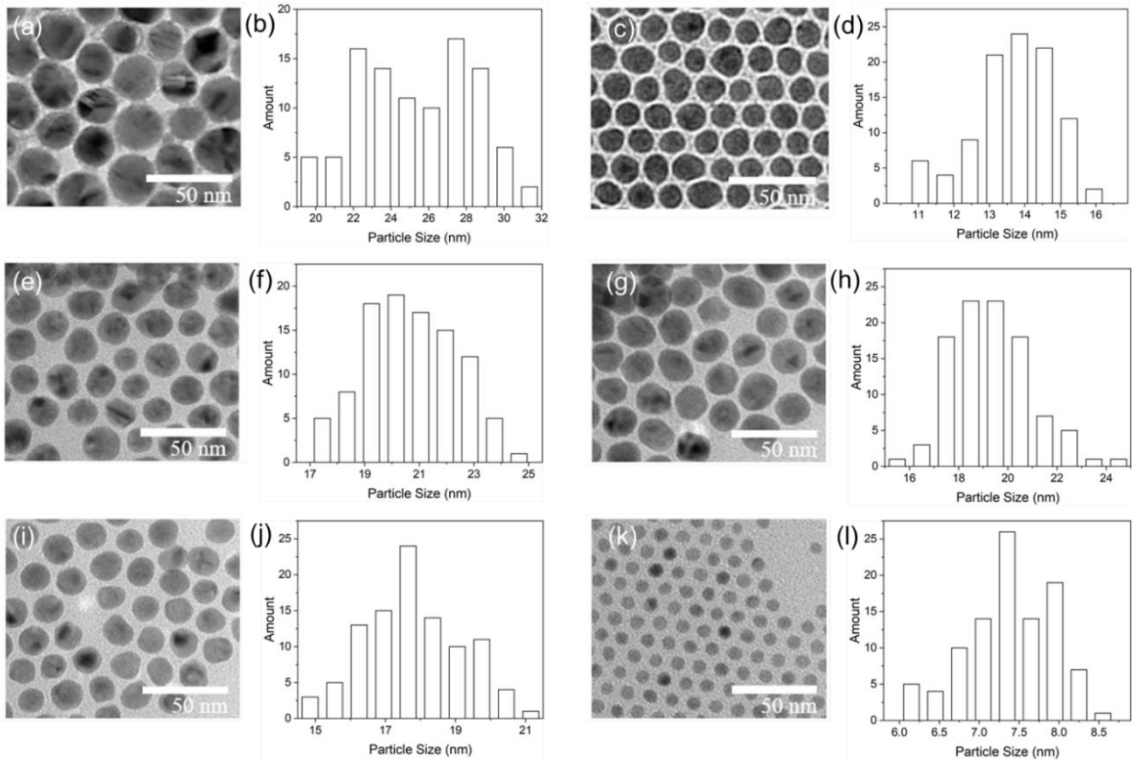

Figure S1. TEM images and size distribution of (**a**,**b**) Cu; (**c**,**d**) $Cu_{0.81}Ni_{0.19}$; (**e**,**f**) $Cu_{0.71}Ni_{0.29}$; (**g**,**h**) $Cu_{0.63}Ni_{0.37}$; (**i**,**j**) $Cu_{0.39}Ni_{0.61}$ and (**k**,**l**) Ni NPs.

Table S1. Sizes of Cu_xNi_{1-x} NPs.

Sample	Size (nm)
Cu	25.4 ± 6.0
$Cu_{0.81}Ni_{0.19}$	13.7 ± 2.6
$Cu_{0.71}Ni_{0.29}$	20.7 ± 3.9
$Cu_{0.63}Ni_{0.37}$	19.3 ± 4.8
$Cu_{0.39}Ni_{0.61}$	17.3 ± 3.2
Ni	7.4 ± 1.3

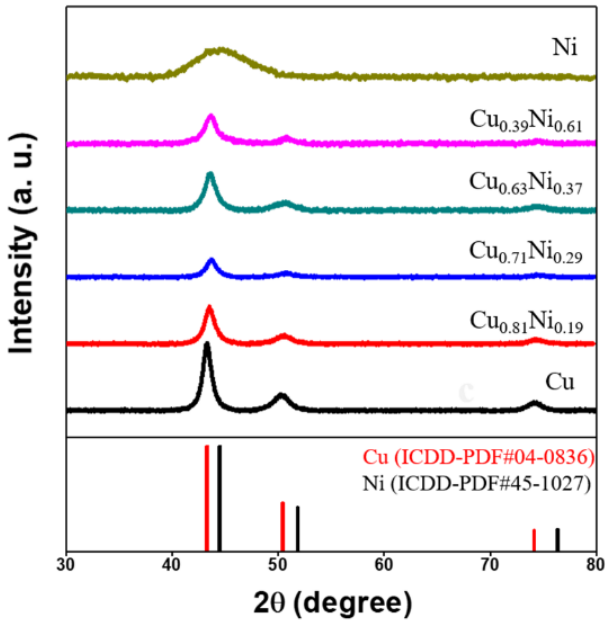

Figure S2. XRD patterns from 30 to 80 degree of Cu_xNi_{1-x} with Cu and Ni references.

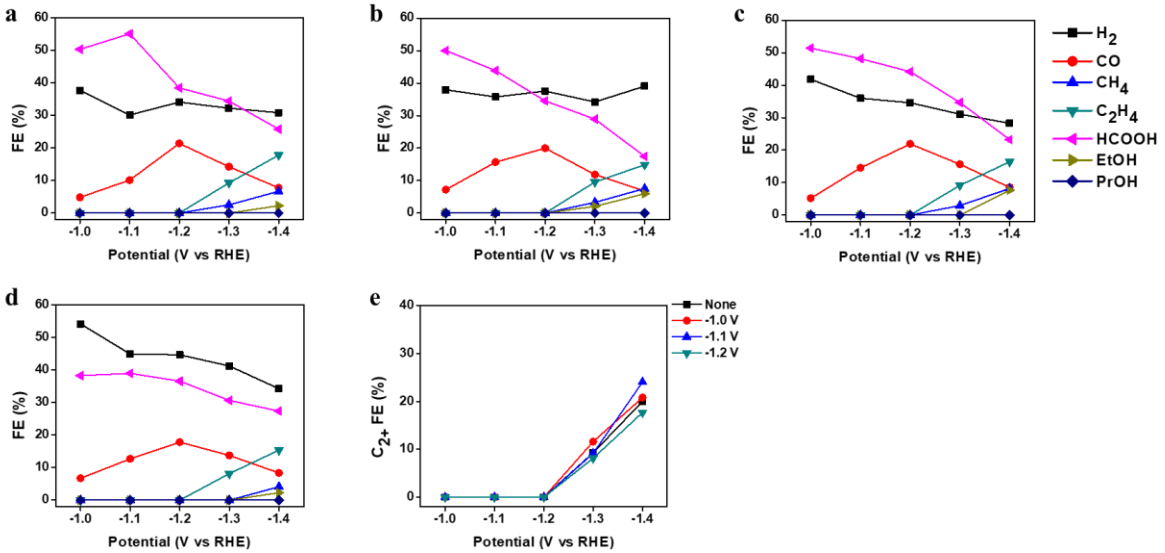

Figure S3. Optimization of the activation step for pure Cu. (**a**) No activation step. (**b**) Activation at −1.0 V_{RHE}. (**c**) Activation at −1.1 V_{RHE}. (**d**) Activation at −1.2 V_{RHE}. (**e**) C_{2+} products FE.

Table S2. C_{2+} FE in the optimization of the activation step for pure Cu (the optimized condition is highlighted).

Applied Potential \ Activation Potential	Without Activation	-1.0 V (vs. RHE)	-1.1 V (vs. RHE)	-1.2 V (vs. RHE)
-1.0 V (vs. RHE)	0	0	0	0
-1.1 V (vs. RHE)	0	0	0	0
-1.2 V (vs. RHE)	0	0	0	0
-1.3 V (vs. RHE)	9.3	11.6	9.2	8.1
-1.4 V (vs. RHE)	20.0	20.8	24.1	17.7

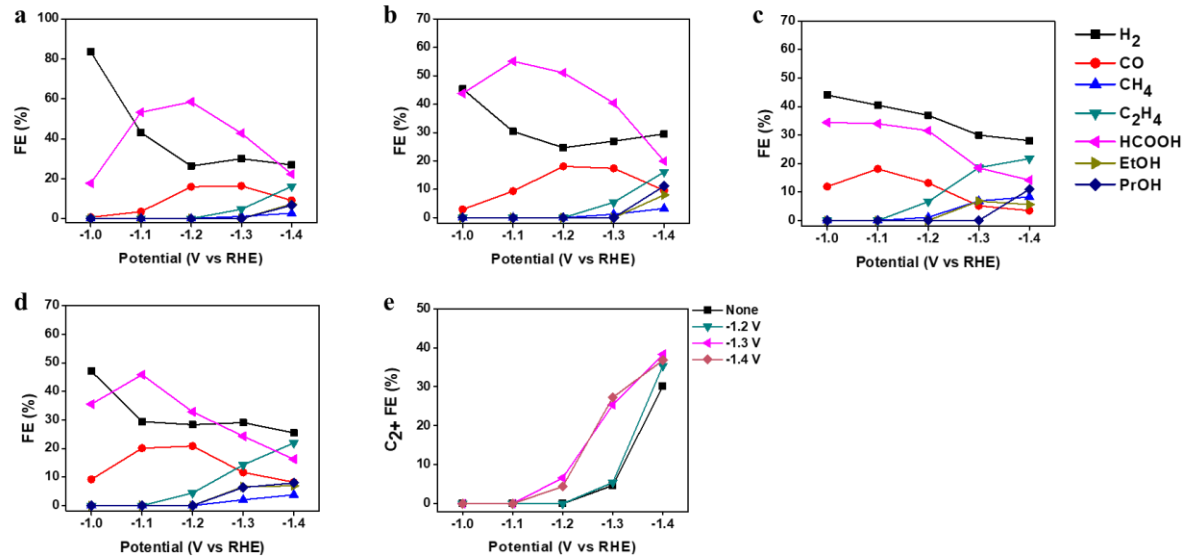

Figure S4. Optimization of the Activation step for $Cu_{0.81}Ni_{0.19}$. (**a**) No activation step. (**b**) Activation at −1.2 V_{RHE}. (**c**) Activation at −1.3 V_{RHE}. (**d**) Activation at −1.4 V_{RHE}. (**e**) C_{2+} products FE.

Table S3. C_{2+} FE in the optimization of the activation step for pure $Cu_{0.81}Ni_{0.19}$ (the optimized condition is highlighted).

Applied Potential \ Activation Potential	Without Activation	-1.2 V (vs. RHE)	-1.3 V (vs. RHE)	-1.4 V (vs. RHE)
-1.0 V (vs. RHE)	0	0	0	0
-1.1 V (vs. RHE)	0	0	0	0
-1.2 V (vs. RHE)	0	0	6.6	4.4
-1.3 V (vs. RHE)	4.7	5.5	25.4	27.3
-1.4 V (vs. RHE)	30.1	35.3	38.3	36.8

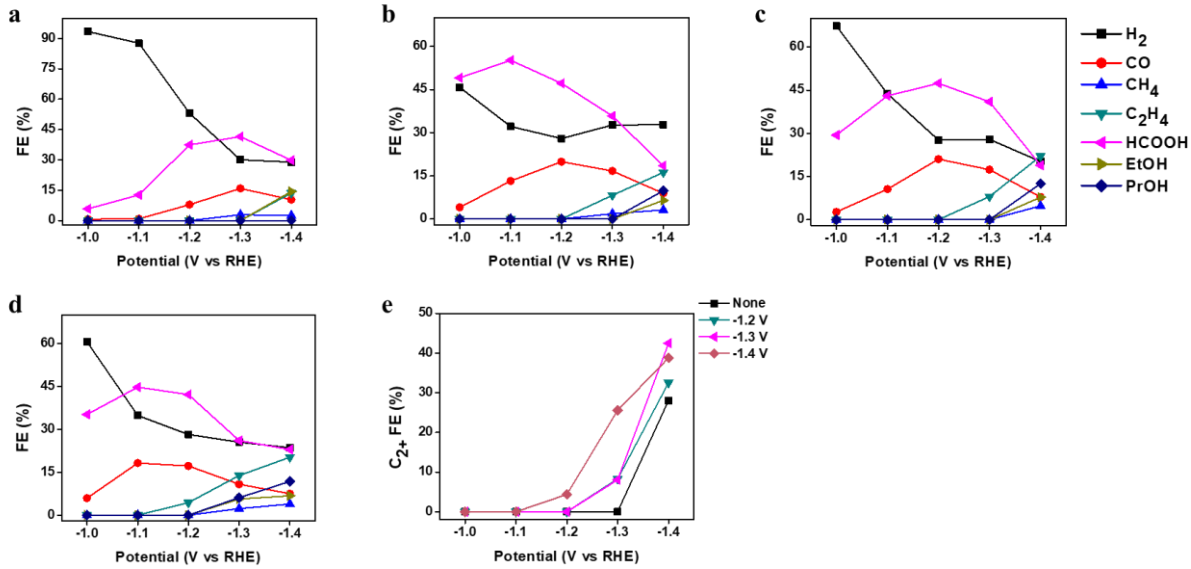

Figure S5. Optimization of the Activation step for $Cu_{0.71}Ni_{0.29}$. (**a**) No activation step. (**b**) Activation at −1.2 V_{RHE}. (**c**) Activation at −1.3 V_{RHE}. (**d**) Activation at −1.4 V_{RHE}. (**e**) C_{2+} products FE.

Table S4. C_{2+} FE in the optimization of the activation step for pure $Cu_{0.71}Ni_{0.29}$ (the optimized condition is highlighted).

Applied Potential \ Activation Potential	Without Activation	-1.2 V (vs. RHE)	-1.3V (vs. RHE)	-1.4 V (vs. RHE)
-1.0 V (vs. RHE)	0	0	0	0
-1.1 V (vs. RHE)	0	0	0	0
-1.2 V (vs. RHE)	0	0	0	4.4
-1.3 V (vs. RHE)	0	8.3	8.1	25.6
-1.4 V (vs. RHE)	28.1	32.5	42.5	38.8

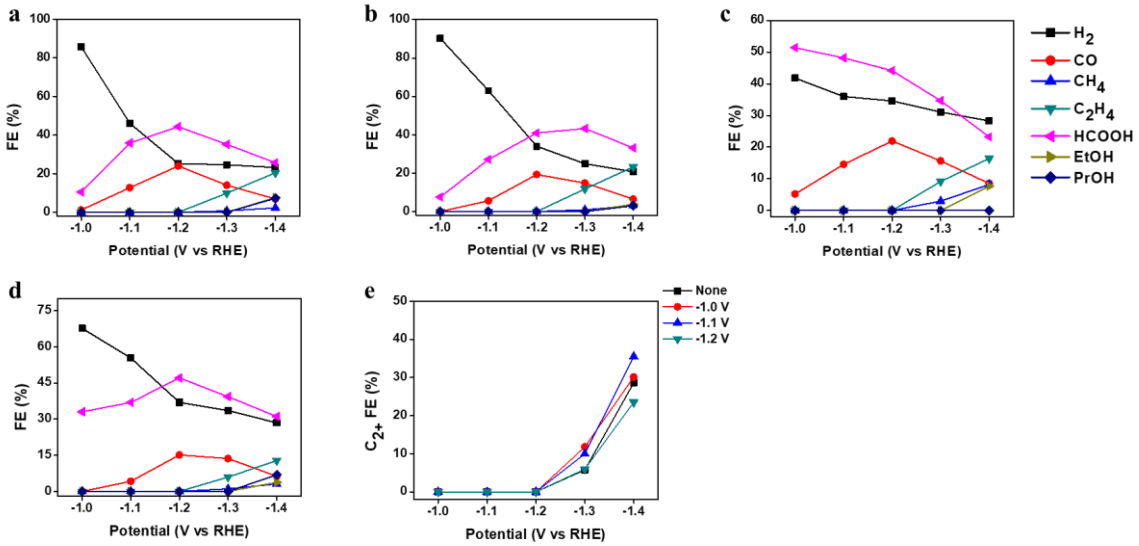

Figure S6. Optimization of the Activation step for $Cu_{0.63}Ni_{0.37}$. (**a**) No activation step. (**b**) Activation at −1.0 V_{RHE}. (**c**) Activation at −1.1 V_{RHE}. (**d**) Activation at −1.2 V_{RHE}. (**e**) C_{2+} products FE.

Table S5. C_{2+} FE in the optimization of the activation step for pure $Cu_{0.63}Ni_{0.37}$ (the optimized condition is highlighted).

Applied Potential \ Activation Potential	Without Activation	-1.0 V (vs. RHE)	-1.1V (vs. RHE)	-1.2 V (vs. RHE)
-1.0 V (vs. RHE)	0	0	0	0
-1.1 V (vs. RHE)	0	0	0	0
-1.2 V (vs. RHE)	0	0	0	0
-1.3 V (vs. RHE)	5.8	11.8	10.0	6.0
-1.4 V (vs. RHE)	28.6	30.1	35.5	23.5

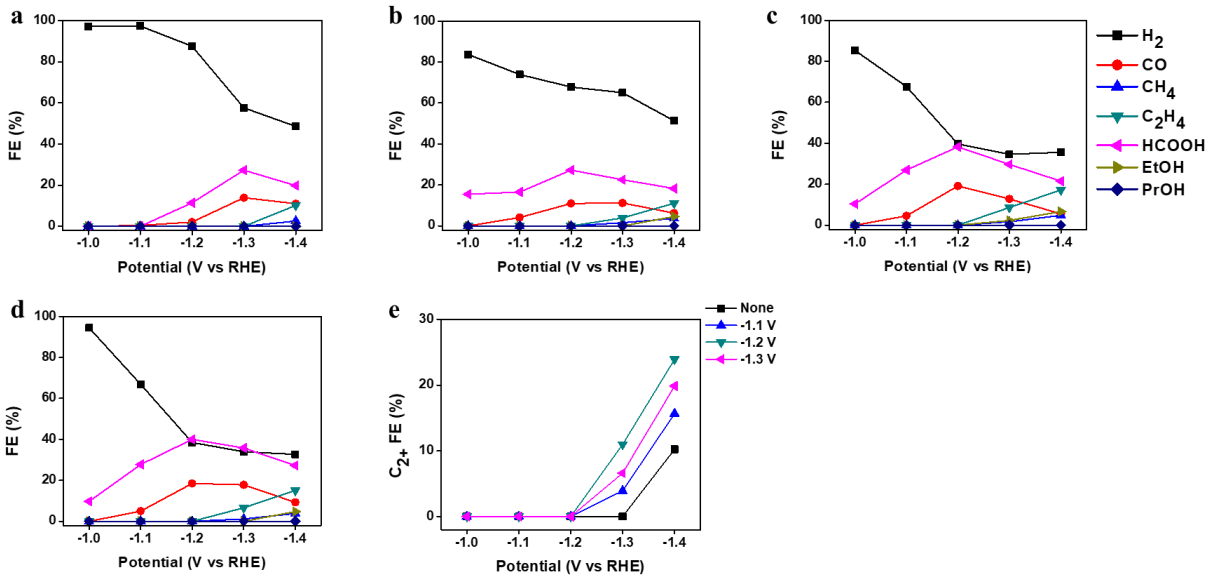

Figure S7. Optimization of the Activation step for $Cu_{0.39}Ni_{0.61}$. (**a**) No activation step. (**b**) Activation at −1.1 V_{RHE}. (**c**) Activation at −1.2 V_{RHE}. (**d**) Activation at −1.3 V_{RHE}. (**e**) C_{2+} products FE.

Table S6. C_{2+} FE in the optimization of the activation step for pure $Cu_{0.39}Ni_{0.61}$ (the optimized condition is highlighted).

Applied Potential \ Activation Potential	Without Activation	-1.1 V (vs. RHE)	-1.2V (vs. RHE)	-1.3 V (vs. RHE)
-1.0 V (vs. RHE)	0	0	0	0
-1.1 V (vs. RHE)	0	0	0	0
-1.2 V (vs. RHE)	0	0	0	0
-1.3 V (vs. RHE)	0	3.9	11.0	6.6
-1.4 V (vs. RHE)	10.2	15.7	23.9	19.9

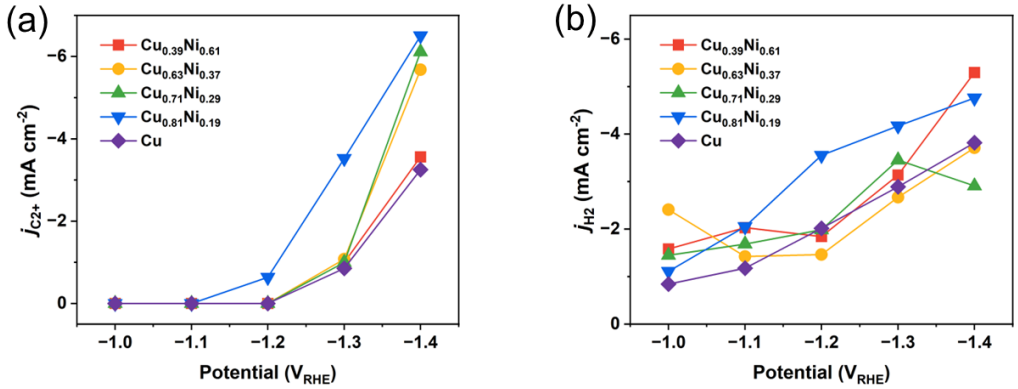

Figure S8. Geometric surface area-normalized current density of Cu_xNi_{1-x} during CO_2RR. (**a**) Partial current density of C_{2+} products (j_{C2+}) at different applied potential. (**b**) Partial current density of H_2 (j_{H2}) at different applied potential.

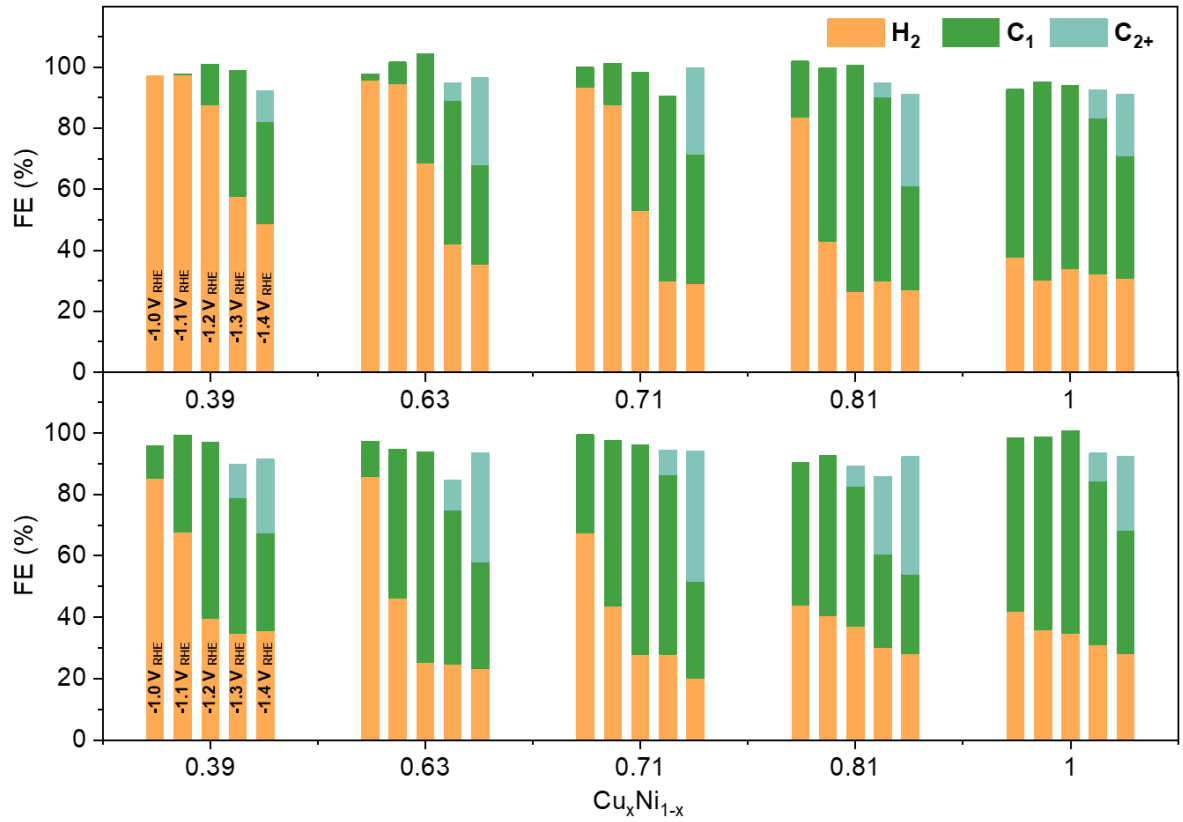

Figure S9. FEs of H_2, C_1 and C_{2+} for Cu_xNi_{1-x} before (top) and after (bottom) activation at optimized potential.

Table S7. Atomic composition of Figures 4 and S11.

Sample	Condition	Cu (%)	Ni (%)	O (%)	Cu: Ni
$Cu_{0.71}Ni_{0.29}$	Pristine	52.0 ± 3.0	24.9 ± 1.5	22.7 ± 1.3	67.6: 32.4
	Activation	76.0 ± 6.0	13.7 ± 1.4	10.3 ± 0.7	84.7: 15.3
	Full scan	87.0 ± 7.0	N/A	13.4 ± 1.2	100: 0
Cu	Pristine	80.0 ± 6.0	N/A	20.0 ± 1.6	N/A
	Activation	59.0 ± 4.0	N/A	41.0 ± 3.0	N/A
	Full scan	62.0 ± 4.0	N/A	38.0 ± 2.0	N/A

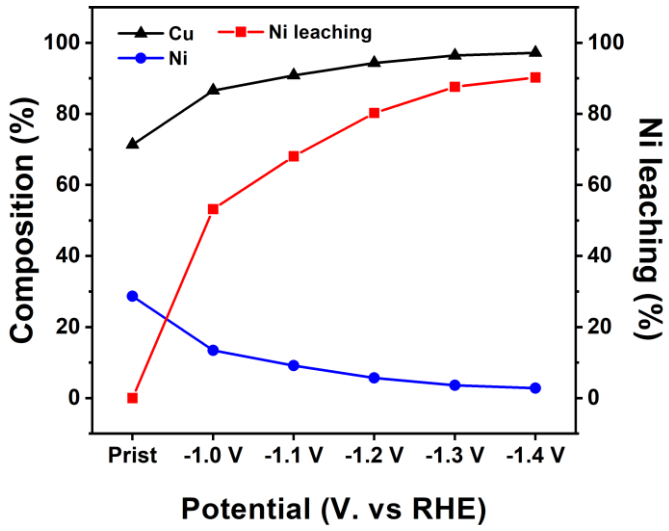

Figure S10. Composition change and Ni leaching percentage of $Cu_{0.71}Ni_{0.29}$ under different activation potentials. (The black and blue line are the composition change of Cu and Ni, respectively; the red line is the Ni leaching percentage).

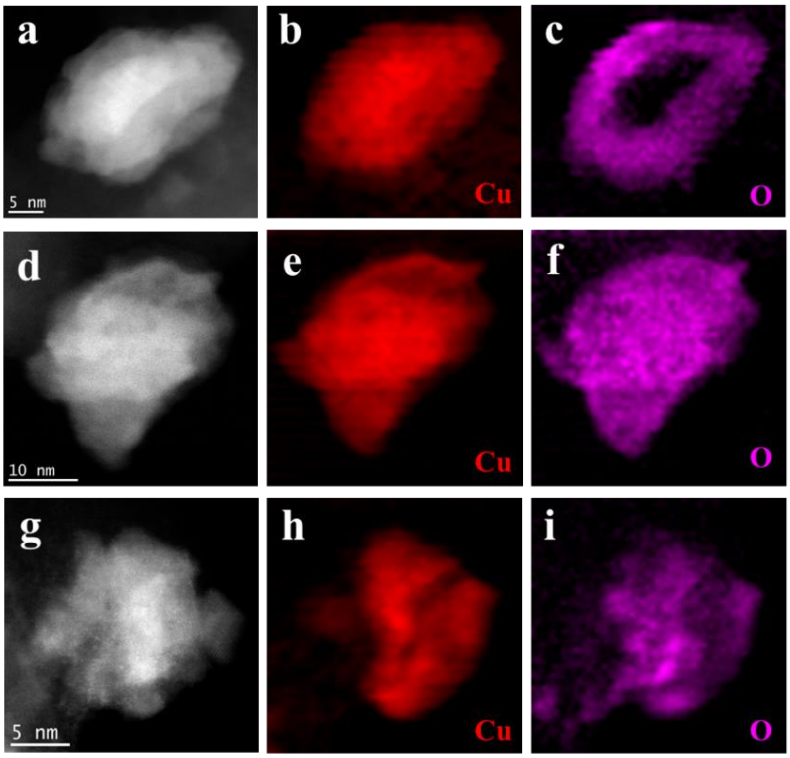

Figure S11. HAADF-STEM and corresponding STEM-EELS elemental maps of pure Cu. (**a**–**c**) Before activation. (**d**,**e**) After activation for 2 h. (**g**–i) After CO_2RR for 5 h.

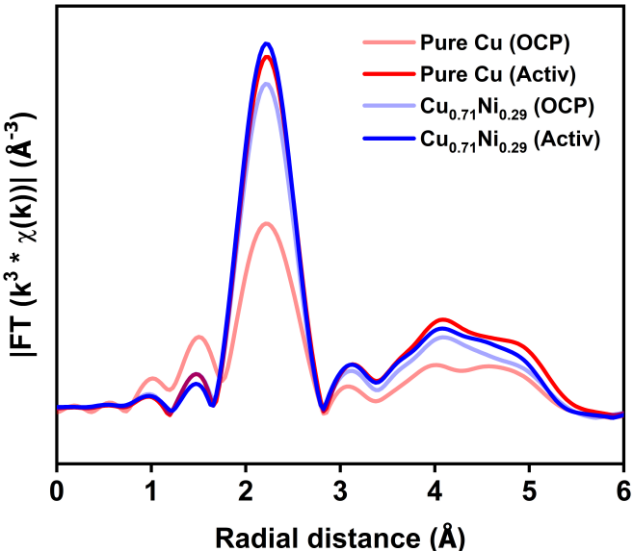

Figure S12. Comparison in k^3-Weighted Cu K-edge *in-situ* EXAFS spectra of pure Cu and $Cu_{0.71}Ni_{0.29}$ at OCP and after activation at their optimized activation potential.

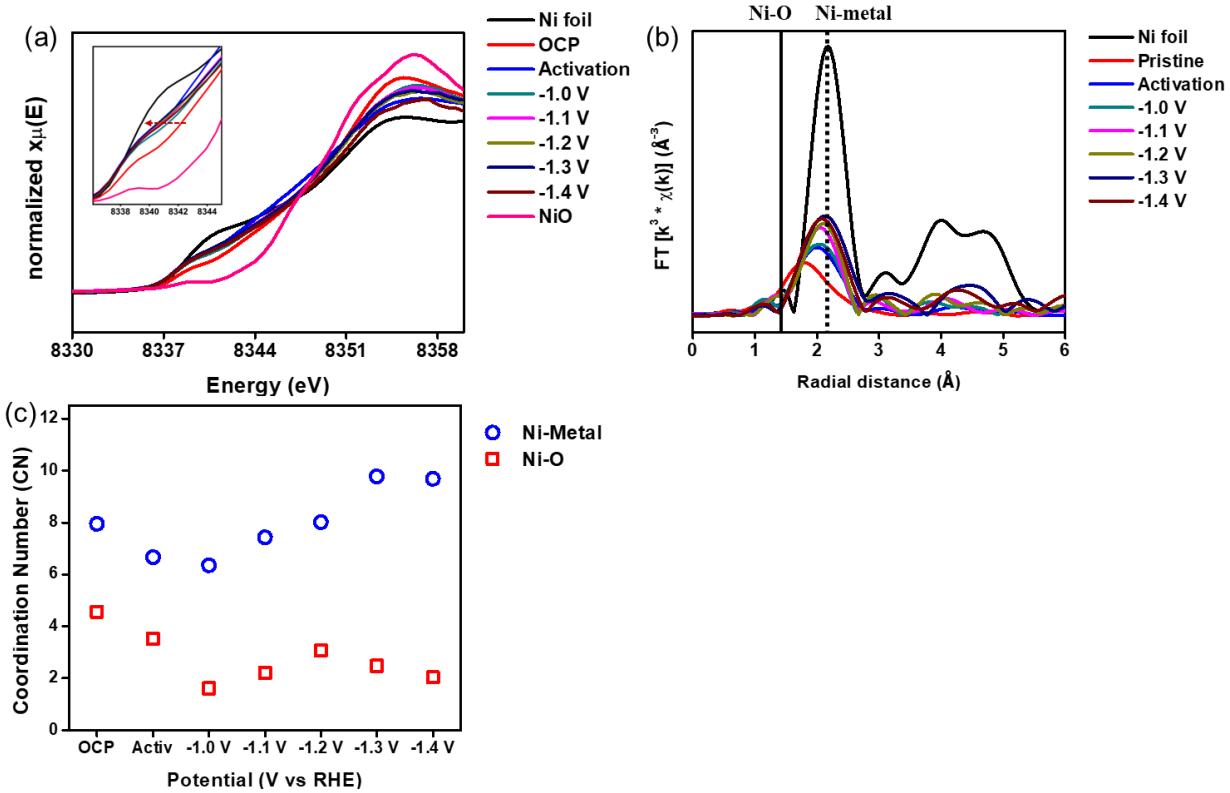

Figure S13. (**a**) XANES of $Cu_{0.71}Ni_{0.29}$, Ni scan. (**b**) Fourier Transformed EXAFS of $Cu_{0.71}Ni_{0.29}$, Ni scan. (**c**) CN of $Cu_{0.71}Ni_{0.29}$, Ni scan.

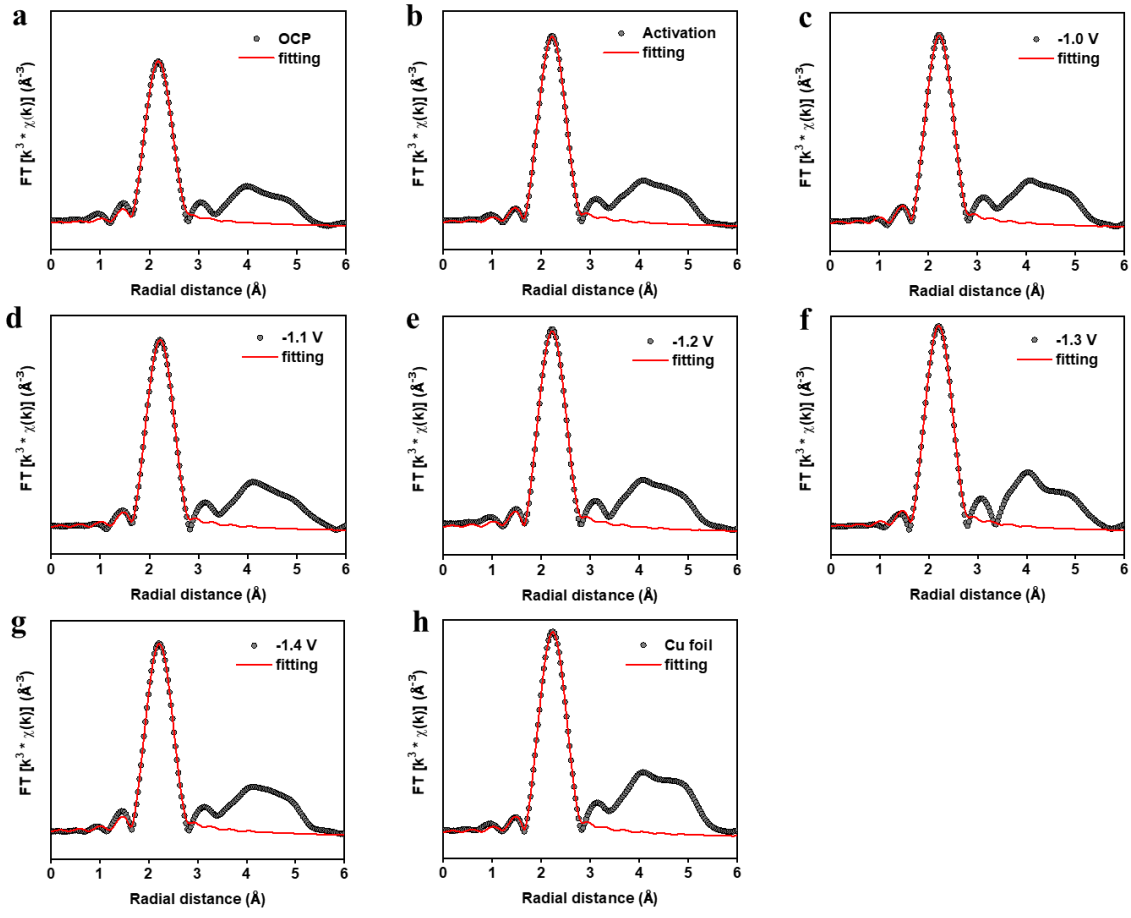

Figure S14. (**a**–**h**) Fourier Transformed EXAFS fitting of $Cu_{0.71}Ni_{0.29}$ at different activation potential, and Cu foil.

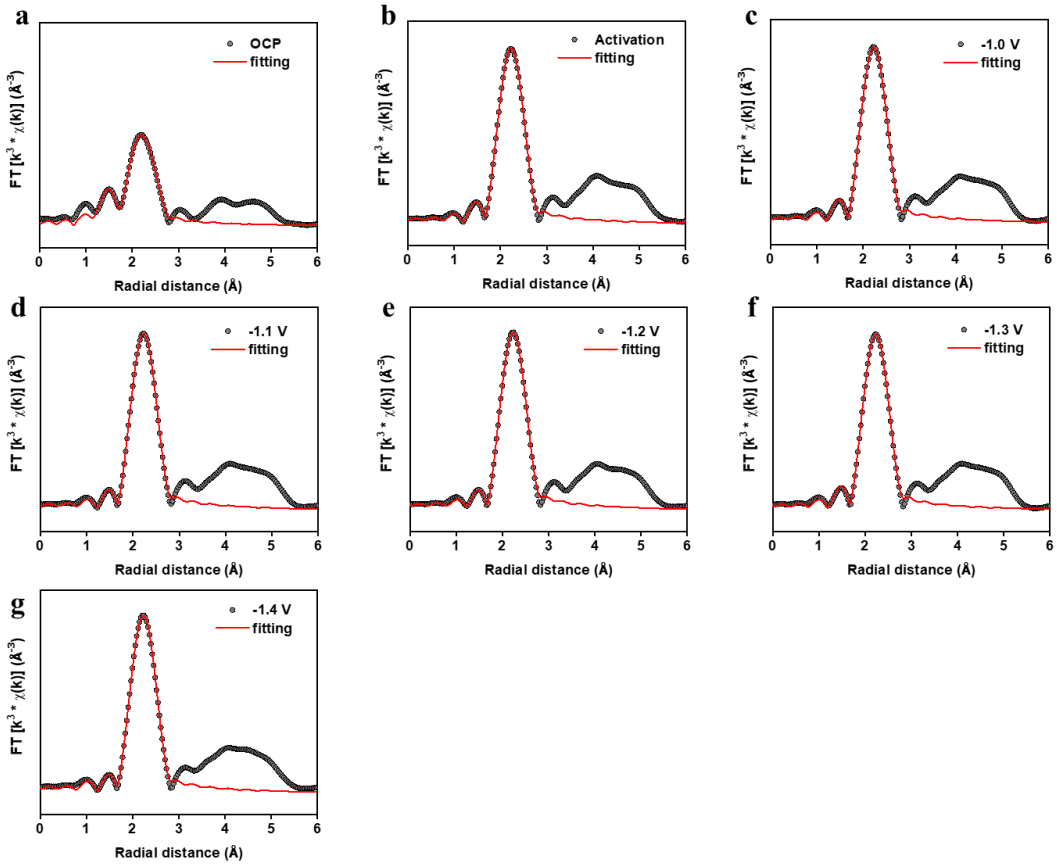

Figure S15. Fourier Transformed EXAFS fitting of pure Cu at different activation potentials.

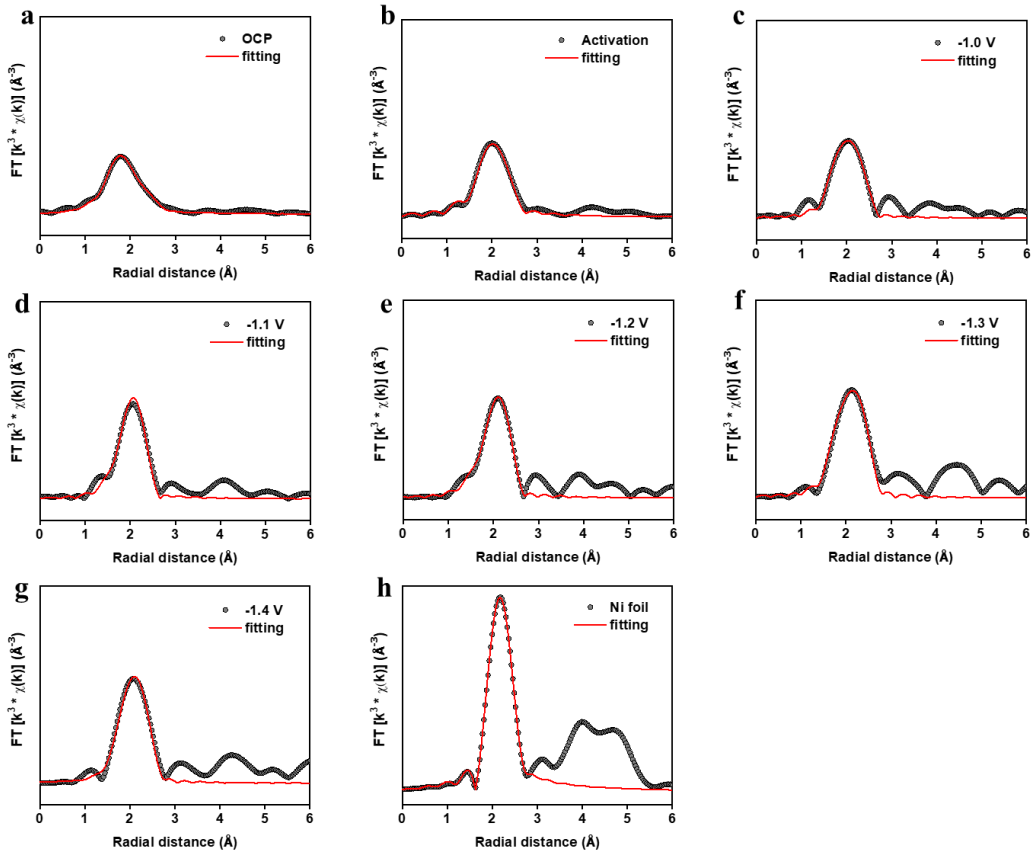

Figure S16. Fourier Transformed EXAFS fitting of $Cu_{0.71}Ni_{0.29}$, Ni scan and Ni foil.

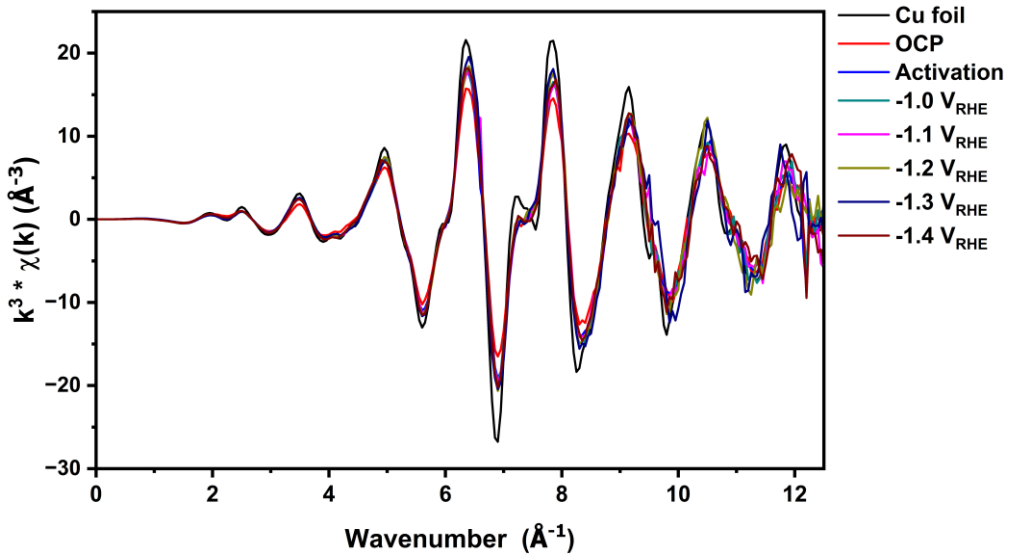

Figure S17. EXAFS oscillation functions at the Cu K-edge of $Cu_{0.71}Ni_{0.29}$ at different conditions and Cu foil reference.

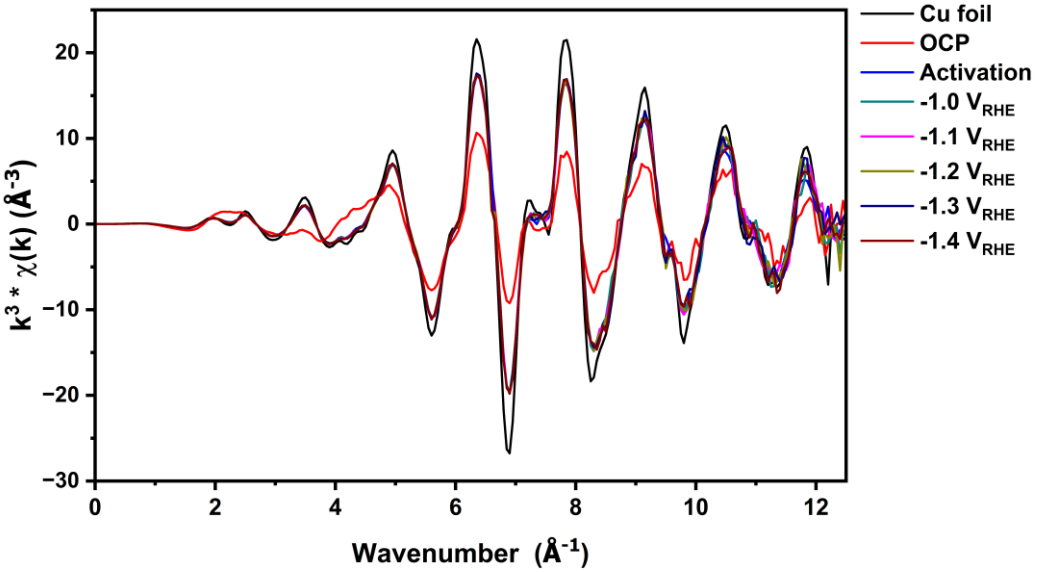

Figure S18. EXAFS oscillation functions at the Cu K-edge of pure Cu at different conditions and Cu foil reference.

Table S8. Fitting parameters of $Cu_{0.71}Ni_{0.29}$, Cu scan.

Sample	Path	S_0^2	CN	R/Å	σ^2 (10^{-3}*Å^2)	ΔE$_0$/eV	R-Factor
Cu foil	Cu-Cu	0.892 ± 0.005	12	2.544 ± 0.001	8.64 ± 0.06	4.066 ± 0.245	0.0002
Pristine	Cu-Cu/Ni	0.892	9.28 ± 0.61	2.534 ± 0.004	8.87 ± 0.51	−2.590 ± 0.769	0.0011
	Cu-O	0.892	0.32 ± 0.31	1.911 ± 0.069	5.51 ± 9.14	1.441 ± 3.827	
Activation	Cu-Cu/Ni	0.892	10.39 ± 0.32	2.534 ± 0.002	8.95 ± 2.39	3.864 ± 0.348	0.0003
	Cu-O	0.892					
−1.0 V$_{RHE}$	Cu-Cu/Ni	0.892	10.29 ± 0.22	2.535 ± 0.001	8.77 ± 0.16	4.186 ± 0.239	0.0002
	Cu-O	0.892					
−1.1 V$_{RHE}$	Cu-Cu/Ni	0.892	10.91 ± 0.42	2.532 ± 0.002	9.32 ± 0.30	3.788 ± 0.439	0.0004
	Cu-O	0.892					
−1.2 V$_{RHE}$	Cu-Cu/Ni	0.892	10.19 ± 0.54	2.533 ± 0.003	8.35 ± 0.40	3.909 ± 0.604	0.0007
	Cu-O	0.892					
−1.3 V$_{RHE}$	Cu-Cu/Ni	0.892	11.03 ± 1.38	2.561 ± 0.007	8.81 ± 0.92	2.347 ± 1.368	0.0038
	Cu-O	0.892					
−1.4 V$_{RHE}$	Cu-Cu/Ni	0.892	10.62 ± 0.52	2.530 ± 0.003	9.04 ± 0.38	3.343 ± 0.558	0.0007
	Cu-O	0.892					

Table S9. Fitting parameter of pure Cu, Cu scan.

Sample	Path	S_0^2	CN	R/Å	σ^2 (10^{-3}*Å^2)	ΔE_0/eV	R-Factor
Cu foil	Cu-Cu	0.892 ± 0.005	12	2.544 ± 0.001	8.64 ± 0.06	4.066 ± 0.245	0.0002
Pristine	Cu-Cu	0.892	5.54 ± 0.34	2.549 ± 0.004	8.79 ± 0.50	−0.804 ± 0.761	0.0024
	Cu-O	0.892	1.91 ± 0.48	1.932 ± 0.019	7.76 ± 2.60	5.463 ± 3.349	
Activation	Cu-Cu	0.892	10.19 ± 0.47	2.540 ± 0.003	8.90 ± 0.361	4.193 ± 0.527	0.0003
	Cu-O	0.892					
−1.0 V_{RHE}	Cu-Cu	0.892	9.85 ± 0.57	2.561 ± 0.003	8.63 ± 0.44	4.204 ± 0.651	0.0002
	Cu-O	0.892					
−1.1 V_{RHE}	Cu-Cu	0.892	9.72 ± 0.22	2.540 ± 0.001	8.47 ± 0.17	4.146 ± 0.263	0.0003
	Cu-O	0.892					
−1.2 V_{RHE}	Cu-Cu	0.892	9.64 ± 0.43	2.541 ± 0.003	8.37 ± 0.34	4.225 ± 0.507	0.0004
	Cu-O	0.892					
−1.3 V_{RHE}	Cu-Cu	0.892	10.08 ± 0.43	2.541 ± 0.003	8.70 ± 0.331	3.831 ± 0.489	0.0009
	Cu-O	0.892					
−1.4 V_{RHE}	Cu-Cu	0.892	10.17 ± 0.42	2.541 ± 0.003	8.78 ± 0.32	4.217 ± 0.464	0.0004
	Cu-O	0.892					

Table S10. Fitting parameters of $Cu_{0.71}Ni_{0.29}$, Ni scan.

Sample	Path	S_0^2	CN	R/Å	σ^2 (10^{-3}*Å^2)	ΔE_0/eV	R-Factor
Ni foil	Ni-Ni	0.800 ± 0.005	12	2.48 ± 0.003	5.95 ± 0.11	6.627 ± 0.531	0.0002
Pristine	Ni-Ni/Cu	0.800	7.95 ± 3.59	2.522 ± 0.025	18.07 ± 4.31	−6.277 ± 3.913	0.0012
	Ni-O	0.800	4.56 ± 1.26	2.083 ± 0.023	9.13 ± 3.30	3.399 ± 2.602	
Activation	Ni-Ni/Cu	0.800	6.66 ± 0.30	2.463 ± 0.011	11.03 ± 0.48	−4.975 ± 1.921	0.0128
	Ni-O	0.800	3.52 ± 0.89	2.049 ± 0.025	2.55 ± 5.334	6.286 ± 7.293	
−1.0 V_{RHE}	Ni-Ni/Cu	0.800	6.35 ± 3.05	2.509 ± 0.033	10.83 ± 4.03	−3.386 ± 6.421	0.0282
	Ni-O	0.800	1.61 ± 1.31	2.073 ± 0.049	1.16 ± 6.1	7.263 ± 9.874	
−1.1 V_{RHE}	Ni-Ni/Cu	0.800	7.43 ± 2.19	2.480 ± 0.018	10.1 ± 2.27	−8.334 ± 3.566	0.0171
	Ni-O	0.800	2.20 ± 0.53	2.068 ± 0.038	8.34 ± 2.38	−0.040 ± 5.806	
−1.2 V_{RHE}	Ni-Ni/Cu	0.800	8.01 ± 1.38	2.501 ± 0.015	10.65 ± 0.55	−4.097 ± 3.010	0.0056
	Ni-O	0.800	3.07 ± 1.78	2.085 ± 0.057	10.81 ± 8.01	3.607 ± 8.381	
−1.3 V_{RHE}	Ni-Ni/Cu	0.800	9.77 ± 2.51	2.549 ± 0.020	11.56 ± 2.19	3.979 ± 3.669	0.0225
	Ni-O	0.800	2.48 ± 0.63	2.105 ± 0.037	2.98 ± 1.05	10.857 ± 6.292	
−1.4 V_{RHE}	Ni-Ni/Cu	0.800	9.68 ± 1.88	2.520 ± 0.012	11.93 ± 1.92	0.172 ± 1.971	0.0084
	Ni-O	0.800	2.03 ± 0.34	2.103 ± 0.031	2.98 ± 1.21	9.953 ± 3.439	

References

1. Gao, Q.; Yan, Z.; Zhang, W.; Pillai, H.S.; Yao, B.; Zang, W.; Liu, Y.; Han, X.; Min, B.; Zhou, H.; et al. Atomic layers of B2 CuPd on Cu nanocubes as catalysts for selective hydrogenation. *J. Am. Chem. Soc.* **2023**, *145*, 19961–19968.
2. Weng, Z.; Wu, Y.; Wang, M.; Jiang, J.; Yang, K.; Huo, S.; Wang, X.F.; Ma, Q.; Brudvig, G.W.; Batista, V.S.; et al. Active sites of copper-complex catalytic materials for electrochemical carbon dioxide reduction. *Nat. Commun.* **2018**, *9*, 415.
3. Ravel, B.; Newville, M. ATHENA, ARTEMIS, HEPHAESTUS: Data analysis for X-ray absorption spectroscopy using IFEFFIT. *J. Synchrotron Radiat.* **2005**, *12*, 537–541.
4. Han, X.; Mou, T.; Liu, S.; Ji, M.; Gao, Q.; He, Q.; Xin, H.; Zhu, H. Heterostructured Bi-Cu_2S nanocrystals for efficient CO_2 electroreduction to formate. *Nanoscale Horiz.* **2022**, *7*, 508–514.
5. Dutta, N.; Bagchi, D.; Chawla, G.; Peter, S.C. A guideline to determine faradaic efficiency in electrochemical CO_2 reduction. *ACS Energy Lett.* **2024**, *9*, 323–328.
6. Peng, C.; Ma, J.; Luo, G.; Yan, S.; Zhang, J.; Chen, Y.; Chen, N.; Wang, Z.; Wei, W.; Sham, T.-K.; et al. (111) Facet-oriented Cu_2Mg Intermetallic Compound with Cu_3-Mg Sites for CO_2 Electroreduction to Ethanol with Industrial Current Density. *Angew. Chem. Int. Ed*. **2024**, *63*, e202316907.